Journal of Power Sources 660 (2025) 238468

Contents lists available at ScienceDirect

Journal of Power Sources

journal homepage: www.elsevier.com/locate/jpowsour

$LiNi_{0.5}Mn_{1.5}O_4$ from aqueous slurry and chitosan-based binder: when high performance meets sustainability

Francesco Falciani [a], Denise Gregucci [a], Luca Bargnesi [a,1], Antonio De Marco [b], Andrea Chiatto [b], Giampaolo Lacarbonara [a,b,*], Catia Arbizzani [a,b,**]

[a] National Interuniversity Consortium of Materials Science and Technology (INSTM), via G. Giusti, 9, 50121, Firenze, Italy
[b] University of Bologna, Department of Chemistry "Giacomo Ciamician", via P. Gobetti 85, 40129, Bologna, Italy

HIGHLIGHTS

- $LiNi_{0.5}Mn_{1.5}O_4$ as high-voltage, sustainable, Co-free cathode.
- Organic solvent is replaced by water in electrode preparation.
- Chitosan/tragacanth mixture is used as bio-derived binder.
- Only tetraethylammonium salt (50 mM $TEAPF_6$) is used as additive in Li metal cell.

GRAPHICAL ABSTRACT

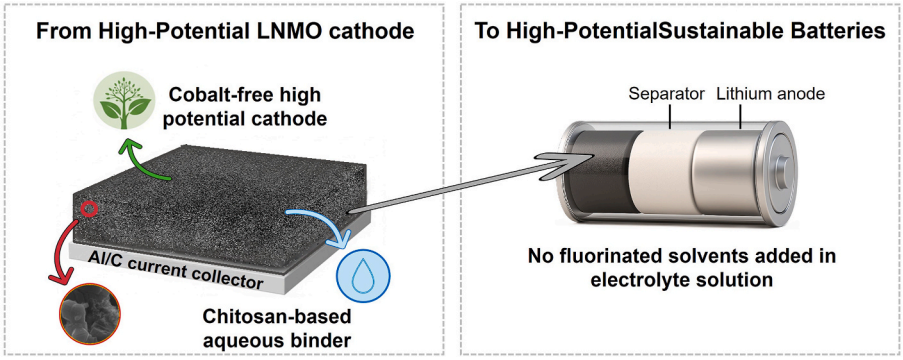

ARTICLE INFO

Keywords:
$LiNi_{0.5}Mn_{1.5}O_4$
LNMO
1,3-Dioxolane
$TEAPF_6$ additive
Chitosan binder
Tragacanth gum

ABSTRACT

Strategies for simultaneously producing high-performance electrochemical energy storage systems with sustainable processes are in the spotlight. The first obvious approach is using Co-free cathodes; the second one is the substitution of organic solvent with water in electrode production, with the further improvement of using bio-derived binders. With $LiNi_{0.5}Mn_{1.5}O_4$ (LNMO), a Co-free, high-potential cathode material, we prepare electrodes with chitosan-based binders to assess their performance in Li metal cells with the conventional electrolytic medium that does not contain other fluorinated compounds but the salt. Usually, fluoroethylene carbonate is added in high-voltage cells, instead of vinylene carbonate, to improve anode interface stability. In order to make use of Li metal anode for maximizing the specific power and energy of the cell, we introduce tetraethylammonium hexafluorophosphate, an additive to ameliorate dendrite growth. Additionally, the effect of 1,3-dioxolane (DOL) in the electrolytic mixture is evaluated as an additive able to produce a thin protective layer of poly(1,3)-dioxolane on LNMO by in situ polymerization. The electrodes are characterized by standard electrochemical methods, and the electrochemical study is completed with physicochemical tests and postmortem analyses to

* Corresponding author. University of Bologna, Department of Chemistry "Giacomo Ciamician", via P. Gobetti 85, 40129, Bologna, Italy.
** Corresponding author. University of Bologna, Department of Chemistry "Giacomo Ciamician", via P. Gobetti 85, 40129, Bologna, Italy.
E-mail addresses: giampaol.lacarbonar2@unibo.it (G. Lacarbonara), catia.arbizzani@unibo.it (C. Arbizzani).
[1] Present affiliation: Centre for Cooperative Research on Alternative Energies (CICenergiGUNE), Basque Research and Technology Alliance (BRTA), Alava Technology Park, Albert Einstein 48, 01510 Vitoria-Gasteiz, Spain.

https://doi.org/10.1016/j.jpowsour.2025.238468
Received 9 July 2025; Received in revised form 8 September 2025; Accepted 21 September 2025
Available online 29 September 2025

assess the feasibility of these sustainable electrodes and the effectiveness of the additives for the stability and cycle life of the material.

1. Introduction

The development of high-performance and sustainable electrochemical systems has been increasingly important. The performance of the batteries on the market (Generation 3) must be improved to achieve the requirements expected in 2030, and academic and industrial research developments are necessary [1]. Defining strategies that simultaneously enable the realization of high-performance electrochemical energy storage systems and their production through sustainable processes, emphasizing the valorization of green materials, has become the most demanding challenge. The automotive market demands higher and higher specific and volumetric energy and power, which can be currently pursued using high-potential cathodes and Li metal or Si-based anodes. On the other hand, climate change is out loud requiring more attention towards the use of critical raw materials, toxic solvents, and fluorinated compounds. Materials and processes sustainability can be achieved by limiting or avoiding the presence of cobalt in cathode materials, and using water-based binders for electrode preparation instead of the conventional, organic ones. The latter strategy, well established for graphite electrodes at industrial level, is technically demanding in the case of cathode materials due to the presence of aluminum current collector, which can corrode, and the possibility of metal ion leaching in the slurries [2,3].

One of the most interesting Co-free cathode materials is $LiNi_{0.5}Mn_{1.5}O_4$ (LNMO), which has been widely studied in the past decade for the high-potential and the good theoretical specific capacity [4]. It has been demonstrated that the specific capacity of graphite//LNMO cell is higher (>10 %) than that of graphite//NMC622, and even higher (>3 %) than that of graphite//NMC811. More importantly, in LNMO the capacity from Ni is totally exploited, with a capacity of LNMO near 44 Ah mol^{-1} of Ni, 37 % and 30 % more than the capacity per mol of Ni of NMC622 and NMC811, respectively [5]. LNMO crystallizes in two types of structures, the ordered $P4_332$ phase and the disordered $Fd\overline{3}m$ phase, depending on synthesis conditions and thermal treatments [6–8]. The ordered phase is characterized by Ni and Mn regularly positioned in 4a and 12d sites, respectively, and only Mn^{4+}, not taking part in the electrochemical process, is present. On the contrary, Mn^{3+} is also present in the disordered phase, and Ni and Mn were randomly distributed on 16d sites [9–11]. However, it has been experimentally demonstrated that the classification of LNMO in two (ordered and disordered) phases could be too simplified [5,12].

The presence of Mn^{3+} diversely affects the electrochemical performance of LNMO. On one hand, the ionic radius of Mn^{3+}, bigger than that of Mn^{4+}, enhances Li^+ movement inside the crystal lattice, which increases rate capability. On the other hand, the disproportionation reaction of Mn^{3+} in Mn^{2+} and Mn^{4+} is responsible for the loss of capacity, Mn^{2+} being dissolved in the electrolyte solution.

Several strategies have been pursued to increase LNMO stability, without affecting capacity and rate capability. They can be viewed as chemical changes, like those in stoichiometry or occurring by doping elements [4–7], or physical changes, by producing a protective coating. Chemical changes are mainly aimed at increasing the intrinsic stability of the crystal lattice. As an example, a disordered LNMO phase ($LiNi_{0.483}Mn^{III}_{0.034}Mn^{IV}_{1.483}O_4$) with only one fourth of the Mn (III) typically present in the conventional disordered phase has been proven to be stable over cycling and to be suitable for application in full cells with graphite [5].

Physical changes are expected to produce physical favourable paths that can improve the charge transfer, or barriers that prevent unwanted reaction and cation release. Very recently, the formation of a $LiAl_5O_8$ surface layer that penetrates along the grain boundaries and forms a neural-like network was carried out on another Co-free electrode material, $Li_{1.2}Mn_{0.6}Ni_{0.2}O_2$. As a result, the increase of charge/discharge kinetics, Li^+ diffusion rate, electrode conductivity, and interfacial contact were observed [13]. The protective layers can be produced by physical techniques, like atomic layer deposition and chemical vapor deposition, or can grow as cathode electrolyte interphase (CEI) by chemical or electrochemical reaction with the solvent, the salt or the additive used [14–17]. To be effective, the protective layer should be thin and well linked to the LNMO particles. The epitaxial growth of a $LaTMO_3$ (with TM = Ni, Mn) monolayer on LNMO demonstrated that a thermodynamically stable thin layer improves the electrochemical performance and suppresses the dissolution of Ni and Mn [18].

Another strategy to get improved battery performance is the use of "single-crystal" cathodes. However, their practical application still faces many challenges, like irreversible structure degradation and cracks. Also in this case, bulk or surface modification strategies are needed, and in the long run they can have good market prospects [19]. Operando spectroscopic techniques, also carried out with syncrotrone radiation, on LNMO single crystals, shed light on the microscale lattice deformation upon lithiation/delitiation and upon cycling, which affect the macroscale degradation of the electrode and are useful for the design of the material [20]. Alongside energy and power performance and long cycle life, it is mandatory to take into consideration safety, cost-effectiveness, and sustainability [1].

The approach of using water-processable binders proposed by Lee et al. [21] twenty years ago for graphite anodes has been proved to be successful [22,23]. Nowadays, graphite anodes are prepared mainly with a binder based on carboxymethyl cellulose/styrene butadiene rubber (CMC/SBR). On the contrary, the use of aqueous solutions for cathode slurries has been hindered by several factors: the presence of Al current collector, the reactivity of cathode materials with water, and the unwanted metal ion leaching. Nonetheless, LNMO electrodes prepared with water-soluble binders (carboxymethylcellulose, alginate, pullulan, chitosan, carrageenan) have already been investigated [24–30].

In the present paper, we have widened the investigation of LNMO with chitosan-based binders [31,32] to assess the compatibility of electrodes with an electrolytic medium that does not contain fluorinated compounds, such as fluoroethylene carbonate (FEC), to protect the anode. With the idea of assembling Li metal cells in order to maximize specific power and energy, we also investigated the possibility of using suitable additives. The first additive is tetraethylammonium hexafluorophosphate ($TEAPF_6$). It is added to the electrolyte in a very small amount (50 mM) to make the dendrite growth less impactful on Li anode and on the whole cell [33]. The second additive is 1,3-dioxolane (DOL), and in situ polymerization has been promoted during the formation cycles to produce a thin protective CEI of poly(1,3)-dioxolane (pDOL) on LNMO [34–36]. It is worth mentioning that the approaches used in this paper take into consideration cost-effectiveness, safety, and scalability, alongside sustainability.

The electrodes have been characterized with standard electrochemical methods in three-electrode cells, and the electrochemical study has been integrated with physicochemical tests and post-mortem analyses to assess the feasibility of these sustainable electrodes and the effectiveness of the additives for the stability and cycle life of the material.

2. Experimental section

2.1. Chemicals

$LiNi_{0.5}Mn_{1.5}O_4$ (LNMO, NEI Corp. Somerset, NJ, USA), chitosan

(Sigma Aldrich, technical grade from shrimp shells, Merck Life Science S.r.l., Milan, Italy), 2-propanol (Sigma Aldrich, HPLC grade, Merck Life Science S.r.l., Milan, Italy), acetic acid (Sigma Aldrich, ACS grade, Merck Life Science S.r.l., Milan, Italy), tragacanth gum (Sigma Aldrich, Merck Life Science S.r.l., Milan, Italy), xanthan gum (Sigma Aldrich, from Xanthomonas campestris, Merck Life Science S.r.l., Milan, Italy) conductive carbon (C-energy, C-45, Imerys Graphite & Carbon Switzerland SA, Bodio, Switzerland), Li metal chip (Cambridge Energy Solutions Cambridge, United Kingdom, 0.45 mm thick), tetraethyl ammonium hexafluorofosfate ($TEAPF_6$, Fluka, >99 %, Merck Life Science S.r.l., Milan, Italy), 1,3-dioxolane (DOL, Sigma Aldrich, HPLC grade, Merck Life Science S.r.l., Milan, Italy), 1M $LiPF_6$ in ethylene carbonate (EC)/dimethyl carbonate (DMC) 1:1 v/v % (LP30, Solvionic, Toulouse, France), DMC (99+% extra dry, Thermo Scientific VWR International S.r.l, Milan, Italy) Whatman microfiber glass membranes (GF/D, VWR International S.r.l, Milan, Italy), nitric acid (Sigma Aldrich, puriss. p.a. ≥ 65 %, reag. ISO, Merck Life Science S.r.l., Milan, Italy), manganese (Carlo Erba Reagent, standard for atomic absorption, 1 mg/mL, Cornaredo, Itay), nickel (Merck, CertiPUR Nickel standard solution, 1000 mg/L, Merck Life Science S.r.l., Milan, Italy).

2.2. Electrode preparation

Tragacanth and xanthan gums were used in combination with chitosan to overcome the brittleness of chitosan-based binders. The two co-binders were investigated as they exhibit different rheological and physicochemical properties. Xanthan gum significantly increases slurry viscosity and stabilizes particle dispersion, but its pronounced pseudoplasticity can limit particle packing and mass loading [37]. Conversely, tragacanth gum provides higher water retention, film-forming ability, and adhesive properties, enabling compact and cohesive slurries with higher loadings [38,39]. Flow curves of chitosan–tragacanth and chitosan–xanthan aqueous solutions at equal polymer concentration (Fig. S1) confirm their distinct solvent interactions and viscosities, which must be considered during slurry preparation. Samples were prepared by dissolving 350 mg of chitosan-gum polymers in a 5:2 wt ratio in 15 mL of 0.5 wt% acetic acid solution. Rheological tests on polymer solutions were carried out using a Rheolab QC rotational rheometer (Anton Paar, Graz, Austria) equipped with a concentric cylinder cup (CC17) for the chitosan–xanthan solution and a double-gap cup (DG42) for the chitosan–tragacanth solution. For electrode preparation, binder solutions containing 2 % natural gums were prepared as follows: the natural gum (tragacanth or xanthan) was dissolved in MilliQ water, 2-propanol and acetic acid in the ratio 79.75:19.75:0.5 wt % (pH 3), and the solution was kept under stirring for 6 h at RT until it became transparent. Then, chitosan was added and stirred further for 6 h at RT, until the solution became transparent. The resulting pH of the binder solution was 4.30 (Fig. 1a). The pH of solutions and slurries was measured by a PHM210 Standard pH METER Radiometer (Analytical Control De Mori s.r.l., Milano, Italy) and a pH XS - Polymer - S7 electrode (Giorgio Bormac S.r.l., Carpi, Italy). Rheological tests on LNMO–CX and LNMO–CT slurries were performed using an MCR 102 parallel-plate rheometer (Anton Paar, Graz, Austria) with a 25 mm plate (PP-25) and a gap of 0.7 ± 0.2 mm. Slurries were applied onto the lower plate with a syringe, and the upper plate was lowered to contact the sample surface; excess material was trimmed before measurement.

The electrodes were prepared by mixing in the binder solution $LiNi_{0.5}Mn_{1.5}O_4$ and the conductive agent Super C45. The final slurry formulation was 86:7:5:2 of LNMO:Super C45:chitosan:natural gum wt. % ratio. The amount of liquid was adjusted in order to reach a viscosity in the range 300–3000 mPa s at 100-1000 s^{-1} shear rate, suitable for the casting procedure (Fig. S2). As a consequence, the different amounts of solvent required lead to different final solid content, 55 % and 30 %, for the slurries containing tragacanth gum and xanthan gum, respectively. The final pH of the slurries was 4.34.

The slurries were cast on carbon-coated aluminum foil by a mini coater machine (MC 20, Hohsen Corp., Japan) by adjusting the thickness to 12 mil (305 μm) and 10 mil (254 μm) for slurries containing tragacanth and xanthan, respectively. The electrode sheets were dried at RT in air. Hence, the electrodes were punched with a 9 mm-diameter puncher, pressed at 7860 kg cm^{-2} for 1 min with a hydraulic press and dried under dynamic vacuum at 120 °C for 12 h in a glass oven (B-585, Büchi, BUCHI Italia s.r.l, Cornaredo, Italy) (Fig. 1b).

The active material loading of the electrodes containing tragacanth gum and xanthan gum was 8.4 ± 0.6 mg cm^{-2} and 2.6 ± 0.3 mg cm^{-2}, respectively. Electrodes with chitosan–xanthan gum as binder will hereafter be referred to as LNMO-CX, while those with chitosan–-tragacanth gum will be indicated as LNMO-CT.

2.3. Physicochemical characterization

The morphological and structural properties of the different LNMO electrodes were investigated by scanning electron microscopy (SEM) using a ZEISS Crossbeam 550 equipped with a Gemini II field emission (FE-SEM) column. Energy Dispersive Spectra (EDS) were acquired using a Bruker X-Flash 7100 Energy Dispersive Spectrometer. EDS has been used to investigate the homogeneity of the electrode and the Mn/Ni ratio. The latter has been carried out by averaging the results of 15

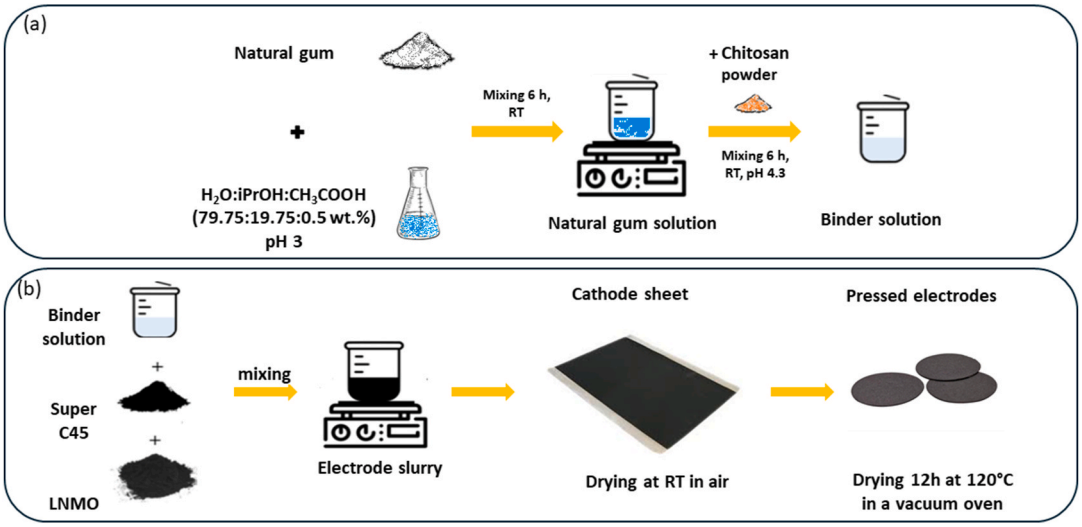

Fig. 1. Schematic representation of the process for obtaining a) the binder solution in aqueous solvent and b) the slurry and the electrodes.

different spots on the sample.

X-ray diffraction (XRD) measurements were carried out with the Empyrean diffractometer (Malvern Panalytical Ltd., Malvern, United Kingdom), with a Cu Kα X-ray tube (Cu LFF-HR), a diffracted beam optic and a 3D detector. The 2θ interval was 5°/80° using an XYZ sample stage. Le Bail refinement was performed to obtain cell parameters.

To evaluate quantitatively the content of Mn and Ni dissolved in the electrolyte, Atomic Emission Microwave Plasma-Atomic Emission Spectrometer (Agilent 4210 MP-AES) was chosen for electrolyte analysis.

2.4. Electrochemical tests

Swagelok T-shaped cells were assembled in a dry box (LabMaster SP, M. Braun Inertgas-Systeme GmbH, Garching, Germany) in argon atmosphere ($H_2O < 0.1$ ppm, $O_2 < 0.1$ ppm), with LNMO working electrodes (we, 9 mm diameter) and lithium metal as counter electrode (ce, 12 mm diameter) and reference electrode (re, 3 mm diameter). The electrolyte was LP30, and the separator was Whatman GF/D. Tests were also carried out by adding 50 mM $TEAPF_6$ to LP30 or 10 μL of an LP30-solution containing 10 wt% of DOL directly on LNMO before sealing the cell. All the electrochemical tests were carried out after 4 h from cell assembly, except those on the cells assembled with DOL, to avoid the unmonitored starting of DOL polymerization. The tests were performed with Perkin-Elmer VMP and Biologic VSP multichannel potentiostat/galvanostats at 30 °C. Cyclic voltammetries (CVs) were carried out in the range 3.5 V and 5.0 V at 50 μV s^{-1}. The rate capability tests were carried out with a constant current/constant potential (CC/CP) protocol and three cycles at C/5, C/2, 1C and again at C/5 rates. The potential range was 3.5 V and 4.85 V (the CP was kept at 4.85 V over 30 min or until the current reached the value corresponding to C/10). Cycling stability was carried out by galvanostatic charge/discharge (GCD) cycles between 3.5 and 4.85 V at 1C with the CC/CP protocol after the rate capability tests or after the first three formation cycles at C/5.

A fast CC/CP protocol at 2C in three-electrode mode was also carried out over 100 cycles for post-mortem analyses of the electrolyte and of the electrodes. In particular, the protocol consisted of 3 formation cycles at C/5, 3 cycles at 1C, and 94 cycles at 2C.

2.5. Post-mortem analyses

Post-mortem analysis was carried out on electrolytes recovered from cells after 100 GCD cycles at 2C rate. The cells were disassembled in an argon-filled dry box. The cathode was rinsed twice with 1 mL of DMC to remove residual electrolyte. The first DMC washing solution was collected and evaporated in an oven at 85 °C to remove the solvent. Separator was first dried under vacuum in the dry-box antechamber for 2.5 h and then digested overnight in 1 mL of 2 % HNO_3 at RT. The dry residual from the electrode first rinsing was redissolved in the acidic separator digestate to obtain a sample representative of the electrolyte. The resulting solution was filtered using 0.22 μm Nylon syringe filter and analyzed using MP-AES 4210 at 403.449 nm and 341.476 nm wavelengths for Mn and Ni detection, respectively. Calibration was performed using multi-element (Mn and Ni) standard solutions with concentrations ranging from 1 to 100 mg/L for Mn and Ni.

3. Results and discussion

The electrochemical comparison of the electrodes was performed by CVs for the LNMO-CX (Fig. 2a) and the LNMO-CT (Fig. 2b). Both electrodes exhibit the characteristic electrochemical features of disordered LNMO, including the Mn^{3+}/Mn^{4+} redox couple at ca. 4.0 V vs Li^+/Li and the two-step $Ni^{2+} \rightarrow Ni^{3+} \rightarrow Ni^{4+}$ oxidation process around 4.7–4.8 V vs Li^+/Li [23]. However, the LNMO-CT electrode displays the most distinct

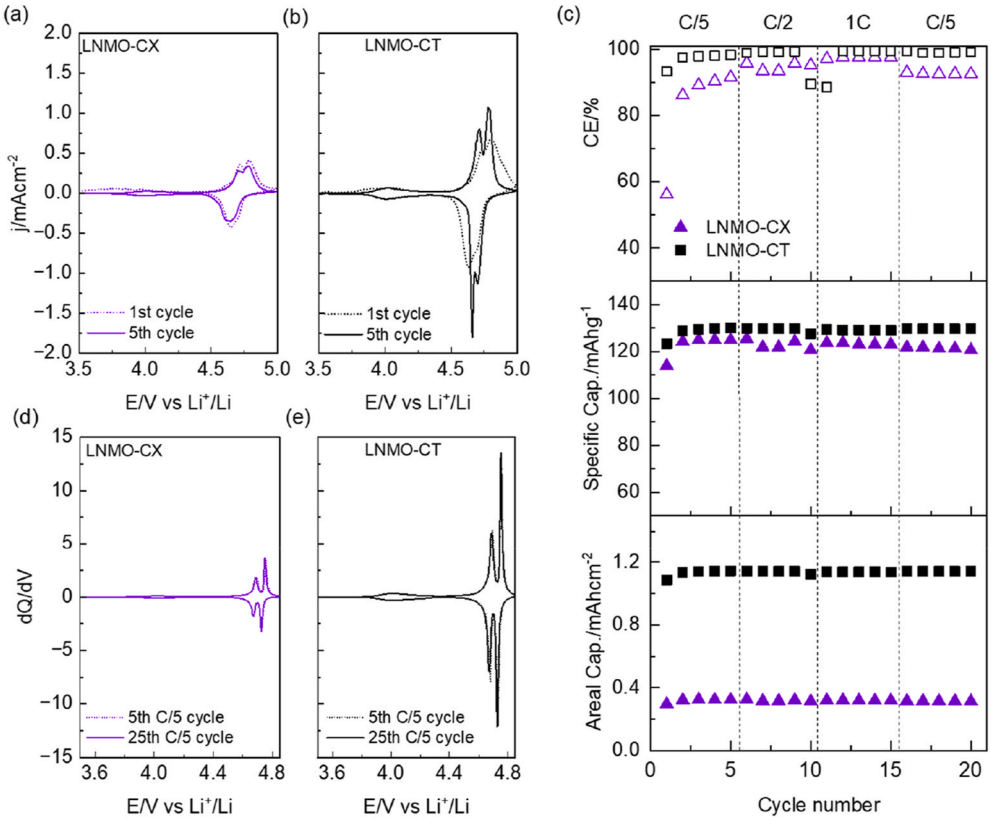

Fig. 2. CVs (1st and 5th cycles) at 0.05 mV s^{-1} of (a) LNMO-CX and (b) LNMO-CT; (c) rate capability results of LNMO electrodes; dQ/dV curves of the 5th and 25th GCD cycle of the rate capability test of (d) LNMO-CX electrodes and (e) LNMO-CT.

redox peaks, particularly for the sequential oxidation and, notably, the reduction of nickel species. In contrast, the LNMO-CX electrode exhibits less well-defined redox features, suggesting more sluggish electron transfer kinetics even if the electrode mass loading is lower. This latter aspect justifies the lower current densities observed for the LNMO-CX compared to those for LNMO-CT. The difference observed in the CVs is also evident in the rate capability tests reported in Fig. 2c. The rate capability of the LNMO-CX and LNMO-CT electrodes was evaluated through galvanostatic cycling at increasing C-rates, ranging from C/5 to 1 C (five cycles per C-rate). Both electrodes deliver high specific capacities, which result unvaried with the C-rate. Especially the LNMO-CT electrode exhibits a specific capacity of 130.0 mAh g^{-1} at C/5 and of 128.9 mAh g^{-1} at 1C. Even if both electrodes exhibited the same specific capacity reported in the LNMO data sheet, it is important to note that the higher solid content achievable with tragacanth gum allows for significantly higher mass loading, resulting in areal capacity nearly three times greater than that of the LNMO-CX electrodes.

Fig. 2d and e shows the differential capacity (dQ/dV) plots obtained by deriving charge with respect to voltage for the C/5 cycles recorded before and after the high-rate cycling, i.e. the 5th and the 25th cycle. These plots exhibit peaks corresponding to those observed in Fig. 2a and b. Notably, the splitting of the peak around 4.7 V vs Li^+/Li is even more pronounced than in the cyclic voltammograms, particularly for LNMO-CX electrodes. The comparison between the 5th and 25th cycle demonstrates the high stability of the electrodes: the nearly perfect overlap of the curves indicates that the electrodes maintain their electrochemical performance even after undergoing rate capability testing up to 1C.

Fig. 3 shows SEM micrographs of LNMO electrodes at different magnifications and cross-sectional views. The binder choice clearly influences both the homogeneity of the composite structure and the resulting electrode morphology.

The LNMO-CX electrodes (Fig. 3a and b) exhibit a less homogeneous and compact distribution of solids compared to the LNMO-CT ones (Fig. 3d and e). Indeed, in the latter, conductive carbon and LNMO particles appear well distributed, exhibiting a uniform microstructure. Conversely, the LNMO-CX electrodes display noticeable heterogeneities and aggregates of conductive carbon at the micron-scale. Also, in the images at high magnification, LNMO-CT again demonstrates superior integration of the nanometric carbon phase, which seems more finely dispersed throughout the electrode matrix. The cross-sectional image of the LNMO-CX electrode (Fig. 3c) reveals a relatively thick and rough structure with microstructural discontinuities. In contrast, the LNMO-CT electrode (Fig. 3f) shows a more compact and uniform thickness, with a tightly packed architecture and well-formed contact with the current collector indicated by the amount of electrode material that remained attached to the current collector when the electrode was bended and broken after the immersion in liquid nitrogen for the cross-section SEM image (Fig. S3). This improved structural homogeneity could justify the best electron transfer kinetics observed in CVs. Since LNMO-CT electrodes outperformed those based on xanthan gum, further investigations are proposed exclusively on LNMO-CT.

Given the better morphology of the LNMO-CT electrode and the possibility to produce electrodes with higher mass loading, further electrochemical investigations were carried out only on LNMO-CT. Long-term stability under high-rate conditions has been evaluated, and Cycling stability over 400 cycles at 1C is reported in Fig. 4a. The electrode showed stable behavior up to 280 cycles, at which point the capacity retention was approximately 94 %, with a capacity fading of 0.02 %/cycle. Beyond this point, instabilities became evident in the coulombic efficiency (CE) trends, which show scattered values. It is important to note that, given the cathode loading and electrode diameter, the 1C current corresponds to 1.3 mA cm^{-2} on the lithium electrode. This represents a quite high current density, at which lithium deposition becomes non-uniform and the deposition/stripping process inefficient, leading to the consumption of the lithium excess present in the cell after a relatively high number of cycles. In Fig. 4b are shown the potential profiles of the two electrochemical processes involved: charge and discharge of the LNMO-CT cathode and lithium deposition-stripping on the lithium anode. The voltage profiles of the cathodes exhibit the characteristic plateaus of LNMO, associated with the oxidation and reduction processes of manganese and nickel. These voltage features are preserved throughout cycling, and the cathodes demonstrate good electrochemical performance even after 396 cycles. Therefore, it is essential to investigate the behavior of the counter electrode to fully understand the cell's overall performance. Focusing on the lithium deposition-stripping is possible to note a higher overpotential on the first cycle that lowers through the cycling due to the lower resistance of the already cycled lithium [33]. At cycle 323, a significant overpotential was observed, indicating issues occurring at the lithium metal surface. Consequently, the lithium electrode was replaced at cycle 325, with a fresh disk. These problems are likely associated with an inhomogeneous solid electrolyte interphase (SEI) and substantial dendrite formation. Finally, at cycle 396, a high overpotential is again observed. The voltage profile at this stage displays features similar to those recorded in the first cycles. This behavior may be due to the deposition and stripping occurring on a younger lithium surface with a lower specific surface area following lithium replacement.

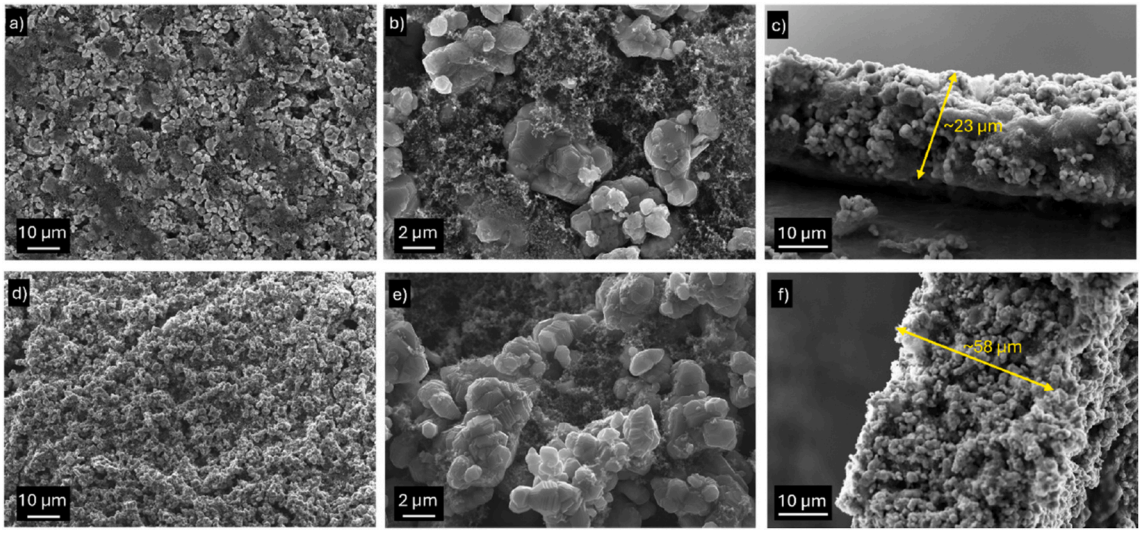

Fig. 3. SEM images of (a–c) LNMO-CX electrode and (d–f) LNMO-CT electrode. Cross-sectional images are reported in images (c) and (f).

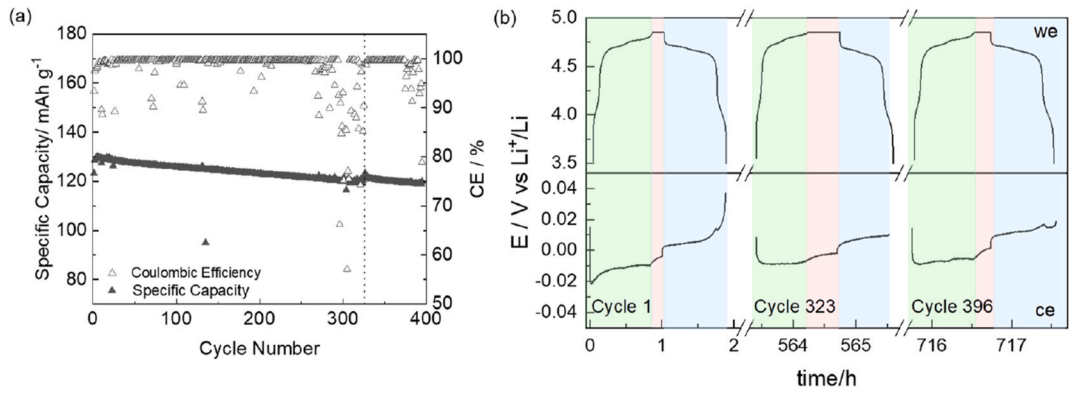

Fig. 4. GCD cycles (a) at 1C of LNMO-CT electrode in half-cell configuration with an active material mass loading of about 8.4 mg cm^{-2}. The dashed line indicates the point at which Li anode has been substituted. Potential profiles (b) of LNMO-CT (we) and lithium (ce) electrodes. Green regions correspond to CC-charge steps, red regions to CP-charge steps, and finally the light blue regions to the CC-discharge steps. (For interpretation of the references to colour in this figure legend, the reader is referred to the Web version of this article.)

The cell then resumed cycling at 1C without additional formation cycles. As observed, both coulombic efficiency and discharge capacity regained stable and consistent values, thus demonstrating that the instability is mainly due to the lithium metal anode working without additives. At the end of the cycling, the capacity retention was 93 % after 400 cycles.

To further enhance cell stability, two different additives were evaluated. We previously reported that ammonium and alkylammonium salts can have a beneficial impact on lithium deposition/stripping by mitigating dendrite growth [33,40]. Among the tested candidates, $TEAPF_6$ was selected as additive, since lithium metal stability results as the limiting factor in the reported stability test.

Additionally, to assist the formation of a stable CEI, pDOL was in situ formed on the LNMO electrode. This was achieved by dropping 10 μL of 10 wt% DOL solution, corresponding to 1 μL of DOL, directly onto the electrode surface during cell assembly. DOL polymerization occurred during the formation cycles of the cell.

Fig. 5a and b shows the 1st and 5th CVs, respectively, of LNMO-CT in the cell containing the additives, compared to those in LP30 of Fig. 2b, here indicated by the black line. Despite the lower currents observed initially, LNMO in electrolytes with additives exhibits well-defined and clearly resolved cathodic and anodic peaks throughout the redox processes comparable to those in LP30 without additives. Notably, the oxidation and reduction peaks of nickel show particularly high resolution, indicating efficient electron transfer and good electrochemical performance, even in the presence of high mass loading and slow electrode wettability.

The rate capability of LNMO-CT electrodes in the electrolytes with the additives was evaluated through GCD cycling at increasing C-rates, ranging from C/5 to 1 C (five cycles per C-rate). The results, compared to those in the absence of additives (black symbols), are shown in Fig. 5c. All three electrolyte systems exhibit excellent specific capacities, with the best performance observed for electrodes tested in the LP30 electrolyte, both neat and with the addition of the $TEAPF_6$ additive. In contrast, slightly lower specific capacities are recorded when using the pDOL-coated electrode. Furthermore, although the delivered specific capacities are comparable between the additive-free system and the one containing $TEAPF_6$, the presence of the additive seems not to affect the cycling performance of LNMO.

Based on these observations, further investigation into the effect of $TEAPF_6$ was conducted by evaluating long-term stability under high-rate conditions. Cycling stability over 400 cycles at 1C is reported in Fig. 6a. The electrode in the electrolyte with $TEAPF_6$ showed stable behaviour with a capacity retention of 86 % after 400 cycles at 1C — evaluated respect to the capacity discharge of the first cycle at 1C after the three formation cycles — and a more stable coulombic efficiency if compared to what was observed in the case of the electrode tested in LP30 reported in Fig. 4a. The voltage profiles shown in Fig. 6b display characteristics similar to those presented in Fig. 4b. However, in this case, the formation of a more homogeneous solid electrolyte interphase (SEI) results in a lower overpotential at both cycle 323 and cycle 396, with lithium deposition-stripping profiles that are highly consistent with each other.

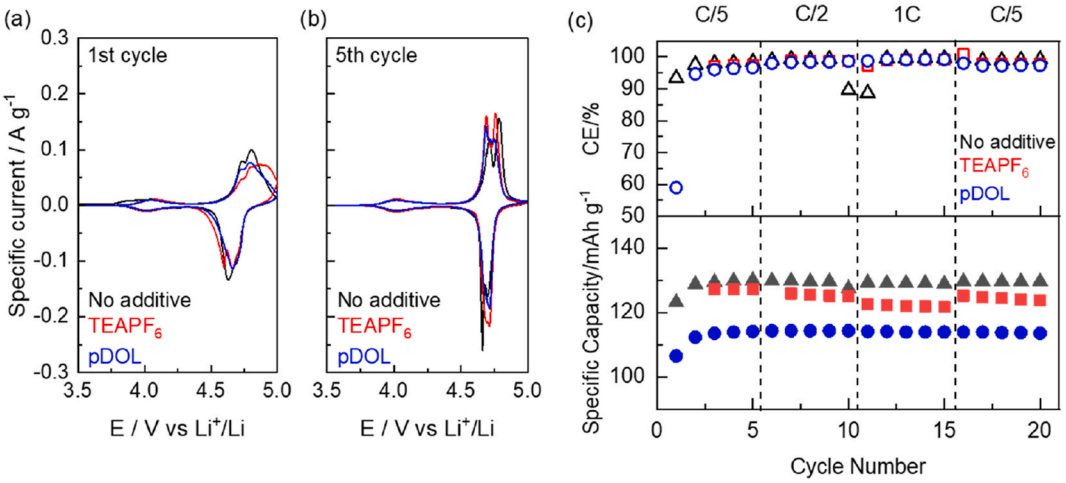

Fig. 5. LNMO-CT electrodes: (a) First and (b) fifth CV at 0.05 mV s^{-1} in the three electrolyte systems, (c) specific capacity and coulombic efficiency.

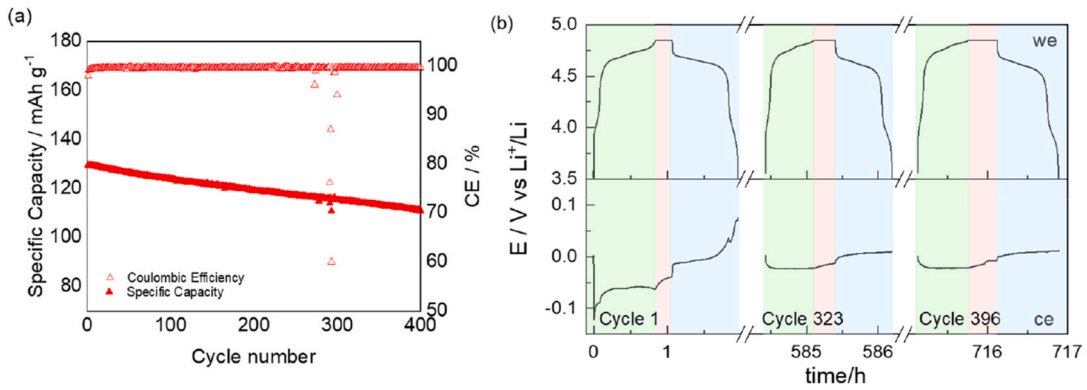

Fig. 6. (a) GCD cycles at 1C of LNMO-CT electrode in half-cell configuration with an active material mass loading of about 8.4 mg cm^{-2} cycled with the electrolyte containing 50 mM $TEAPF_6$. (b) Potential profiles of LNMO-CT (we) and lithium (ce) electrodes. Green regions correspond to CC-charge steps, red regions to CP-charge steps, and finally the light blue regions to the CC-discharge steps. (For interpretation of the references to colour in this figure legend, the reader is referred to the Web version of this article.)

These findings suggest that the presence of the $TEAPF_6$ additive helps to prevent dendrite formation and preserves the surface integrity of the lithium counter electrode, thereby enhancing the stability and lifespan of the cell.

To evaluate the effectiveness of the additives, the electrochemical stability of the three systems was tested by cycling the LNMO-CT electrode at 2C in three-electrode configurations. As shown in Fig. 7a, the cells in neat LP30 and with $TEAPF_6$ exhibit comparable performance, delivering a capacity of approximately 120 mAh g^{-1} at the 100th cycle. Conversely, the LNMO-CT electrode cycled with pDOL shows a lower coulombic efficiency during the first 10 cycles, along with a reduced capacity that progressively fades upon cycling. This behavior suggests that the polymerization of DOL on the electrode surface negatively affects performance, both in terms of capacity values and retention. After the electrochemical tests, the cells were disassembled, and both the separator and cathode were recovered for post-mortem analyses. Specifically, metal dissolution was assessed by MP-AES by analyzing the electrolyte soaked in the separator with the procedure described in the Experimental section. MP-AES was selected due to its capability to quantify metal concentrations in complex liquid matrices with minimal sample preparation, offering an easier alternative to flame-based AAS or more costly ICP techniques.

Fig. 7b shows the concentrations of Mn and Ni in the samples of the three different electrolytes: LP30 without additive, with $TEAPF_6$, and with DOL. These values represent the extent of metal dissolution from the LNMO-CT electrode and are used as indicators of the cathode stability in each electrolyte system. The sample obtained from the cell without the additive shows a moderate level of metal dissolution, especially when compared to the sample with $TEAPF_6$, which exhibits lower Mn and Ni concentrations, indicating improved electrode stabilization. In contrast, the sample from the cell cycled with pDOL shows significantly higher metal dissolution, especially Ni. Therefore, among the three systems, $TEAPF_6$ appears to be the most effective additive in mitigating transition metal dissolution from the LNMO-CT electrode, while pDOL leads to enhanced degradation. These results are fully consistent with the electrochemical experiments.

Changes in morphology and composition, following metal dissolution from LNMO throughout galvanostatic cycling at 2C have been evaluated by SEM and EDS. The latter was conducted by averaging the results of the microanalyses over 15 different spots on the sample, as shown in Fig. S4 and Table S1.

While MP-AES quantifies the extent of metal dissolution into the electrolyte soaked in the separator, EDS offers a surface-sensitive assessment of the remaining metal content on the cathode, enabling a comparative understanding of dissolution versus retention after cycling. Mn/Ni ratios obtained from MP-AES on separators are compared with the EDS results and summarized in Table 1. An increase in the Mn/Ni ratio in the electrolyte indicates preferential Mn dissolution, while a lower Mn/Ni ratio suggests a higher contribution of Ni loss. As shown in Table 1, the Mn/Ni ratio in the pristine electrode is 3.41. After cycling without additives, the AES data show an increased Mn/Ni ratio of 3.91, indicating a preferential dissolution of Mn over Ni, which is consistent with what already reported for LNMO electrodes [41]. The EDS analysis of the corresponding electrode shows a slight decrease in the Mn/Ni

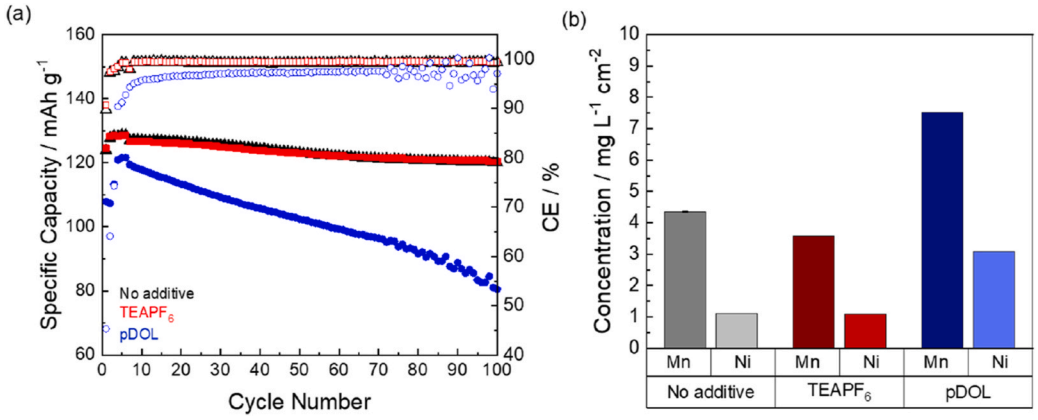

Fig. 7. (a) GCD cycles at 2C of LNMO-CT electrode in three electrode mode with an active material mass loading of about 8.4 mg cm^{-2} with GF/D separator and in the three different electrolytes; (b) MP-AES post-mortem analysis of Mn and Ni concentrations leached by the electrodes.

Table 1
Mn/Ni ratio by MP-AES analyses of metals leached in electrolyte and by EDS analyses of the cycled LNMO-CT electrodes.

	Mn/Ni ratio leached MP-AES	Mn/Ni ratio cycled LNMO EDS
Pristine	/	3.41
No additive	3.91	3.12
$TEAPF_6$	3.31	3.40
pDOL	2.44	3.62

ratio to 3.12, suggesting a Mn depletion from the electrode. In contrast, the electrode cycled in the presence of $TEAPF_6$ exhibits a more balanced Mn/Ni ratio in both AES (3.31) and EDS (3.40), indicating that the additive effectively limits metal dissolution and helps maintain surface composition closer to the pristine state. On the other hand, the electrolyte containing DOL shows a Mn/Ni ratio of 2.44, which is significantly lower than the pristine value, despite a slight increase in surface Mn/Ni ratio (3.62) observed by EDS. This apparent discrepancy suggests that Ni dissolution is more pronounced than Mn in the presence of pDOL on the electrode surface. Additionally, it must be considered that the concentration of metals in the separators is considerably higher, as shown in Fig. 6b, further reinforcing the conclusion that pDOL leads to increased instability of the LNMO-CT electrode.

Fig. 8 shows SEM images of the LNMO-CT electrodes cycled in the three electrolyte systems compared with the pristine one, highlighting the changes in surface morphology and providing insights into the structural stability of the LNMO crystals. The pristine LNMO-CT electrode (Fig. 8a) exhibits well-defined LNMO crystals with sharp edges and plain surfaces, suggesting a high degree of crystallinity. This morphology reflects the as-prepared electrode surface. After 100 cycles in the absence of additive (Fig. 8b), the electrode exhibits larger, more aggregated particles with smoother edges and visible signs of surface roughening. Partial deterioration of the LNMO crystal structure is evident, with the presence of small deposits between particles. In the case of LNMO-CT cycled in the presence of $TEAPF_6$ (Fig. 8c), the electrode surface undergoes significant morphological modification. Numerous spherical aggregates are observed, which, based on EDS analysis (Table S1), are primarily composed of C, N, and F. These features point to the formation of surface layers or decomposition products induced by $TEAPF_6$. Despite the extensive surface coverage, the bulk LNMO crystal structure remains discernible, although cracks are visible in some particles. In the sample cycled in the presence of DOL (Fig. 8d), LNMO particles appear smoother and are covered by thin layers or flake-like features, likely arising from polymeric products or passivation layers formed upon DOL decomposition. Compared to the pristine sample, the LNMO crystals are less faceted and more rounded, suggesting a degree of structural degradation, albeit more pronounced than in the other cases. Overall, these observations suggest that $TEAPF_6$ is compatible with such a high-voltage cathode as LNMO. Further studies, out of the scope of this paper, are ongoing to investigate the nature and the characteristics of SEI on Li.

XRD has been used to reveal structural changes in the LNMO samples after 100 cycles at a high rate, and diffraction patterns are reported in Fig. 8e. The reference peaks of disordered LNMO (cyan, 01-080-2162) were added for a matter of comparison with the obtained diffraction pattern. The aluminum reference (magenta, 00-001-1176) was also included in the plot to better identify the different phases, given that in the diffraction pattern there are also peaks associated with the aluminum current collector. The analysis revealed that all the samples analyzed correspond to disordered LNMO (Fd $\bar{3}$ m) and the only impurity is related to the current collector.

Regarding the electrodes cycled at 2C without additives (black), the diffractogram overlaps almost perfectly with that of the pristine electrode (green). Only a small shift to smaller angles is observed. When additives such as $TEAPF_6$ (red) and DOL (blue) are introduced, a shift of the diffraction peaks toward higher angles is observed—more pronounced in the case of DOL —indicating a unit cell contraction of the LNMO crystal structure following cycling (Table 2 and Fig. S5). These findings align with the SEM observations, where a clear structural collapse is evident in the DOL-containing sample, while the integrity of the structure is maintained in all other samples.

4. Conclusions

In this work, we demonstrate that sustainable, water-processed LNMO cathodes using chitosan-based binders can achieve high electrochemical performance while maintaining environmental compatibility. Although both investigated formulations showed good electrochemical performance, LNMO-CT electrodes, based on a combination of chitosan and tragacanth gum, exhibited improved morphological homogeneity compared to those containing xanthan gum. These features translate into improved electron transport kinetics as observed by CV, higher areal capacities (up to ca. 1.2 mAh cm^{-2}), and outstanding

Table 2
Cell parameters obtained via Le Bail structure refinement.

Sample	Cell parameters (a = b = c) (Å)
Pristine	8.179
No Additive	8.184
$TEAPF_6$	8.160
pDOL	8.126

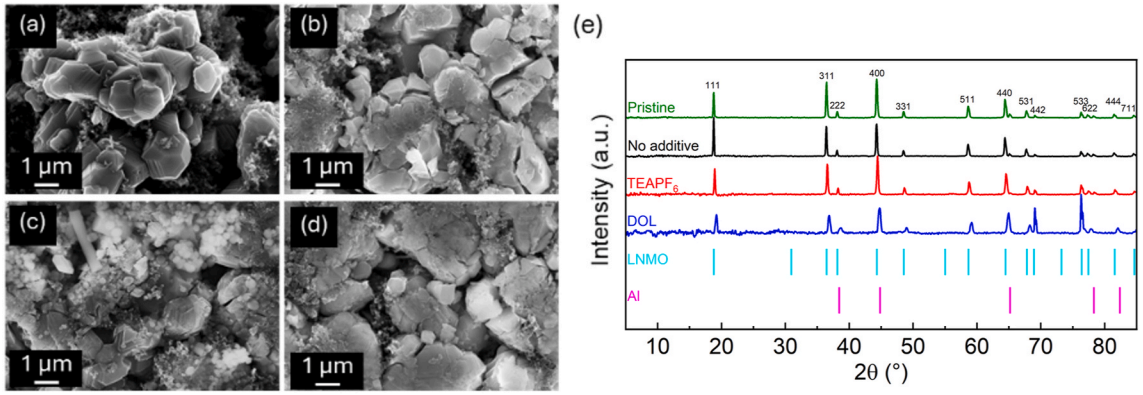

Fig. 8. SEM images of LNMO-CT electrodes: (a) Pristine, (b) after 100 cycles in LP30 without additive, (c) cycled in LP30 - 50 mM $TEAPF_6$, (d) cycled with 1 µL DOL on LNMO surface, (e) XRD diffraction patterns of pristine electrode, electrodes with and without additives after 100 cycles at 2C and reference peak positions of LNMO (cyan, 01-080-2162) and Al (magenta, 00-001-1176). (For interpretation of the references to colour in this figure legend, the reader is referred to the Web version of this article.)

rate performance, with specific capacities ca. 130 mAh g^{-1} at C-rates from C/5 to 1C. Long-term galvanostatic cycling at 1C over 400 cycles confirms their remarkable durability, with capacity retention exceeding 93 %. To further increase the performance in Li full cell, two additives were assessed, $TEAPF_6$ and DOL. The former for stabilizing the Li metal interface, the latter to mitigate cathode degradation by forming an in situ polymerized thin layer of pDOL. $TEAPF_6$ showed clear benefits, improving coulombic efficiency and preserving capacity over extended cycling at high rates (86 % capacity retention after 400 cycles at 1C and 95 % after 100 cycles at 2C), while also effectively limiting Mn and Ni dissolution as confirmed by MP-AES and EDS analyses. In contrast, the in-situ polymerization of DOL led to higher transition metal leaching from the electrode, lower coulombic efficiency, and increasing capacity fading, especially under 2C cycling conditions.

These findings highlight the synergistic potential of bio-derived binder systems and carefully selected non-fluorinated additives to bridge performance and sustainability in next-generation lithium batteries. Future efforts will focus on optimizing additive concentrations and tailoring DOL polymerization.

CRediT authorship contribution statement

Francesco Falciani: Writing – original draft, Visualization, Methodology, Investigation, Formal analysis, Data curation. **Denise Gregucci:** Writing – original draft, Methodology, Investigation, Formal analysis, Data curation. **Luca Bargnesi:** Investigation, Formal analysis, Data curation. **Antonio De Marco:** Writing – original draft, Investigation, Formal analysis, Data curation. **Andrea Chiatto:** Investigation, Data curation. **Giampaolo Lacarbonara:** Writing – original draft, Validation, Methodology, Investigation, Conceptualization. **Catia Arbizzani:** Writing – review & editing, Supervision, Resources, Project administration, Funding acquisition, Conceptualization.

Declaration of competing interest

The authors declare the following financial interests/personal relationships which may be considered as potential competing interests: Given her role as Editor, she had no involvement in the peer review of this article and had no access to information regarding its peer review. Full responsibility for the editorial process for this article was delegated to another journal editor. - C. A. If there are other authors, they declare that they have no known competing financial interests or personal relationships that could have appeared to influence the work reported in this paper.

Acknowledgements

This work has been financed by the Research Fund for the Italian Electrical System (Ministero della Transizione Ecologica-MiTE, DM October 27, 2021 published on G.U.R.I n. 269 - November 11, 2021), within the research project "*ORgANics for Green Electrochemical Energy Storage*" [ORANGEES], approved by MiTE DM of August 05, 2022, published on G.U.R.I. n. 192-18/08/2022, and by the Research Fund for the Italian Electrical System (Ministero dell'Ambiente e della Sicurezza Energetica -MASE) under the Three-Year Research Plan 2025–2027 Decree n. 388 of November 6, 2024 "Approvazione del Piano Triennale 2025–2027 della Ricerca di Sistema elettrico", in compliance with the Decree of 12/04/24, n.139.

Appendix A. Supplementary data

Supplementary data to this article can be found online at https://doi.org/10.1016/j.jpowsour.2025.238468.

Data availability

Data will be made available on request.

References

[1] BEPA strategic research and innovation agenda. https://bepassociation.eu/our-work/sria/. (Accessed 4 September 2025).
[2] D. Bresser, D. Buchholz, A. Moretti, A. Varzi, S. Passerini, Alternative binders for sustainable electrochemical energy storage – the transition to aqueous electrode processing and bio-derived polymers, Energy Environ. Sci. 11 (2018) 3096–3127, https://doi.org/10.1039/C8EE00640G.
[3] T. Rasheed, M.T. Anwar, A. Naveed, A. Ali, Biopolymer based materials as alternative greener binders for sustainable electrochemical energy storage applications, ChemistrySelect 7 (2022) e202203202, https://doi.org/10.1002/slct.202203202.
[4] S. Choi, W. Feng, Y. Xia, Recent progress of high voltage spinel $LiMn_{1.5}Ni_{0.5}O_4$ cathode material for lithium-ion battery: surface modification, doping, electrolyte, and oxygen deficiency, ACS Omega 9 (17) (2024) 18688–18708, https://doi.org/10.1021/acsomega.3c09101.
[5] P. Stüble, V. Mereacre, H. Gebwein, J.R. Binder, On the composition of $LiNi_{0.5}Mn_{1.5}O_4$ cathode active material, Adv. Energy Mater. 13 (2023) 2203778, https://doi.org/10.1002/aenm.202203778.
[6] S. Pateaux, L. Sannier, H. Lignier, Y. Reynier, C. Bourbon, S. Jouanneau, F. Le Cras, S. Martinet, High voltage spinel oxides for Li-ion batteries: from the material research to the application, J. Power Sources 189 (1) (2009) 344–352, https://doi.org/10.1016/j.jpowsour.2008.08.043.
[7] D. Liu, W. Zhu, J. Trottier, C. Gagnon, F. Barray, A. Guerfi, A. Mauger, H. Groult, C. M. Julien, J.B. Goodenough, K. Zaghib, Spinel materials for high-voltage cathodes in Li-ion batteries, RSC Adv. 4 (2014) 154–167, https://doi.org/10.1039/c3ra45706k.
[8] J. Xiao, X. Chen, P.V. Sushko, M.L. Sushko, L. Kovarik, J. Feng, Z. Deng, J. Zheng, J. L. Graff, Z. Nie, D. Choi, J. Liu, J.-G. Zhang, M.S. Whittingham, High-performance $LiNi_{0.5}Mn_{1.5}O_4$ spinel controlled by Mn^{3+} concentration and site disorder, Adv. Mater. 24 (2012) 2109–2116, https://doi.org/10.1002/adma.201104767.
[9] J.H. Kim, S.T. Myung, C.S. Yoon, S.G. Kang, Y.K. Sun, Comparative study of $LiNi_{0.5}Mn_{1.5}O_{4-\delta}$ and $LiNi_{0.5}Mn_{1.5}O_4$ cathodes having two crystallographic structures: Fd-3m and $P4_332$, Chem. Mater. 16 (5) (2004) 906–914, https://doi.org/10.1021/cm035050s.
[10] M. Kunduraci, J.F. Al-Sharab, G.G. Amatucci, High-power nanostructured $LiMn_{2-x}Ni_xO_4$ high-voltage lithium-ion battery electrode materials: electrochemical impact of electronic conductivity and morphology, Chem. Mater. 18 (2006) 3525–3532, https://doi.org/10.1021/cm060729s.
[11] J. Yang, X. Han, X. Zhang, F. Cheng, J. Chen, Spinel $LiNi_{0.5}Mn_{1.5}O_4$ cathode for rechargeable lithium-ion batteries: Nano vs micro, ordered phase ($P4_332$) vs disordered phase (Fd-3m), Nano Res. 6 (9) (2013) 679–687, https://doi.org/10.1007/s12274-013-0343-5.
[12] X. Zhu, A. Huang, I. Martens, N. Vostrov, Y. Sun, M.-I. Richard, T.U. Schülli, L. Wang, High-voltage spinel cathode materials: navigating the structural evolution for lithium-ion batteries, Adv. Mater. 36 (2024) 2403482, https://doi.org/10.1002/adma.202403482.
[13] Y. Cheng, C. Yang, Y. Wang, Q. Tong, Y. Ge, J. Zhu, Y. Jiang, G. Sun, B. Tian, Z. Wang, Z. Yu, Constructing neural-like network channels from the surface to interface for enhanced high-rate cycling stability in Co-free Li-rich cathode, Energy Mater. 5 (2025) 500081, https://doi.org/10.20517/energymater.2024.293.
[14] P. Sun, Y. Ma, T. Zhai, H. Li, High performance $LiNi_{0.5}Mn_{1.5}O_4$ cathode by Al-coating and Al^{3+}-doping through a physical vapor deposition method, Electrochim. Acta 191 (2016) 237–246, https://doi.org/10.1016/j.electacta.2016.01.087.
[15] H. Nakamura, T. Kawaguchi, T. Masuyama, A. Sakuda, T. Saito, K. Kuratani, S. Ohsaki, S. Watano, Dry coating of active material particles with sulfide solid electrolytes for an all-solid-state lithium battery, J. Power Sources 448 (2020) 227579, https://doi.org/10.1016/j.jpowsour.2019.227579.
[16] H. Lee, S. Choi, S. Choi, H.-J. Kim, Y. Choi, S. Yoon, J.-J. Cho, SEI layer-forming additives for $LiNi_{0.5}Mn_{1.5}O_4$/graphite 5 V Li-ion batteries, Electrochem. Commun. 9 (4) (2007) 801–806, https://doi.org/10.1016/j.elecom.2006.11.008.
[17] C. Arbizzani, F. De Giorgio, L. Porcarelli, M. Mastragostino, V. Khomenko, V. Barsukov, D. Bresser, S. Passerini, Use of non-conventional electrolyte salt and additives in high-voltage graphite/$LiNi_{0.4}Mn_{1.6}O_4$ batteries, J. Power Sources 238 (2013) 17–20, https://doi.org/10.1016/j.jpowsour.2013.03.052.
[18] X. Zhu, T.U. Schülli, X. Yang, T. lin, Y. Hu, N. Cheng, H. Fujii, K. Ozawa, B. Cowie, Q. Gu, S. Zhou, Z. Cheng, Y. Du, L. Wang, Epitaxial growth of an atom-thin layer on a $LiNi_{0.5}Mn_{1.5}O_4$ cathode for stable Li-ion battery cycling, Nat. Commun. 13 (2022) 1565, https://doi.org/10.1038/s41467-022-28963-9.
[19] B. You, Z. Wang, F. Shen, Y. Chang, W. Peng, X. Li, H. Guo, Q. Hu, C. Deng, S. Yang, G. Yan, J. Wang, Research progress of single-crystal nickel-rich cathode materials for lithium ion batteries, Small Methods 5 (2021) 2100234, https://doi.org/10.1002/smtd.202100234.
[20] N. Vostrov, I. Martens, M. Colalongo, E. Zatterin, M. Ronovsky, A. Boulineau, S. Leake, X. Zhu, L. Wang, M.-I. Richard, T.U. Schülli, Plastic deformation of $LiNi_{0.5}Mn_{1.5}O_4$ single crystals caused by domain orientation dynamics, Adv. Energy Mater. 15 (2025) 2404933, https://doi.org/10.1002/aenm.202404933.
[21] J.-H. Lee, U. Paik, V.A. Hackley, Y.-M. Choi, Effect of carboxymethyl cellulose on aqueous processing of natural graphite negative electrodes and their

electrochemical performance for lithium batteries, J. Electrochem. Soc. 152 (2005) A1763, https://doi.org/10.1149/1.1979214.
[22] F. Jeschull, D. Brandell, M. Wohlfahrt-Mehrens, M. Memm, Water-soluble binders for lithium-ion battery graphite electrodes: Slurry rheology, coating adhesion, and electrochemical performance, Energy Technol. 5 (2017) 2108–2118, https://doi.org/10.1002/ente.201700200.
[23] M.J. Jolley, T.S. Pathan, C. Jenkins, M.J. Loveridge, Investigating the effect of the degree of cross-linking in styrene butadiene rubber on the performance of graphite anodes for the use in lithium-ion batteries, J. Appl. Polym. Sci. 141 (2024) e55135, https://doi.org/10.1002/app.55135.
[24] F. Bigoni, F. De Giorgio, F. Soavi, C. Arbizzani, New formulations of high-voltage cathodes for Li-Ion batteries with water-processable binders, ECS Trans. 73 (1) (2016) 249–257, https://doi.org/10.1149/07301.0249ecst.
[25] F. Bigoni, F. De Giorgio, F. Soavi, C. Arbizzani, Sodium alginate: a water-processable binder in high-voltage cathode formulations, J. Electrochem. Soc. 164 (1) (2017) A6171–A6177, https://doi.org/10.1149/2.0281701jes.
[26] F. De Giorgio, N. Laszczynski, J. von Zamory, M. Mastragostino, C. Arbizzani, S. Passerini, Graphite//$LiNi_{0.5}Mn_{1.5}O_4$ cells based on environmentally friendly made-in-water electrodes, ChemSusChem 10 (2) (2017) 379–386, https://doi.org/10.1002/cssc.201601249.
[27] M. Kuenzel, D. Bresser, T. Diemant, D. Vieira Carvalho, G.-T. Kim, R. Jürgen Behm, S. Passerini, Complementary strategies toward the aqueous processing of high-voltage $LiNi_{0.5}Mn_{1.5}O_4$ lithium-ion cathodes, ChemSusChem 11 (2018) 562–573, https://doi.org/10.1002/cssc.201702021.
[28] A. Brilloni, F. Marchesini, F. Poli, E. Petri, F. Soavi, Performance comparison of LMNO cathodes produced with pullulan or PEDOT:PSS water-processable binders, Energies 15 (2022) 2608, https://doi.org/10.3390/en15072608.
[29] M. Kuenzel, H. Choi, F. Wu, A. Kazzazi, P. Axmann, M. Wohlfahrt-Mehrens, D. Bresser, S. Passerini, Co-Crosslinked water-soluble biopolymers as a binder for high-voltage $LiNi_{0.5}Mn_{1.5}O_4$|Graphite lithium-ion full cells, ChemSusChem 13 (10) (2020) 2650–2660, https://doi.org/10.1002/cssc.201903483.
[30] M. Binder, E. Keller, D. Bresser, Realization of high mass loading $LiNi_{0.5}Mn_{1.5}O_4$ Li-ion cathodes using water-soluble carrageenan as binder, J. Power Sources 603 (2024) 234487, https://doi.org/10.1016/j.jpowsour.2024.234487.
[31] L. Bargnesi, A. Rozzarin, G. Lacarbonara, S. Tombolesi, C. Arbizzani, Sustainable modification of Chitosan binder for capacitive electrodes operating in aqueous electrolytes, Chemelectrochem 10 (4) (2023) e202201080, https://doi.org/10.1002/celc.202201080.
[32] M. Kuenzel, R. Porhiel, D. Bresser, J. Asenbauer, P. Axmann, M. Wohlfahrt-Mehrens, S. Passerini, Deriving structure-performance relations of chemically modified chitosan binders for sustainable high-voltage $LiNi_{0.5}Mn_{1.5}O_4$ cathodes, Batteries & Supercaps 3 (2020) 155–164, https://doi.org/10.1002/batt.201900140.
[33] D. Di Cillo, L. Bargnesi, G. Lacarbonara, C. Arbizzani, Ammonium and tetraalkylammonium salts as additives for Li metal electrodes, Batteries 9 (2) (2023) 142, https://doi.org/10.3390/batteries9020142.
[34] A. La Monaca, F. De Giorgio, F. Soavi, G. Tarquini, M. Di Carli, P.P. Prosini, C. Arbizzani, 1,3-Dioxolane: a strategy to improve electrode interfaces in lithium ion and lithium-sulfur batteries, Chemelectrochem 5 (2018) 1272–1278, https://doi.org/10.1002/celc.201701348.
[35] N. Albanelli, F. Capodarca, M. Zanoni, G. Lacarbonara, M.L. Focarete, C. Gualandi, C. Arbizzani, Poly(1,3-dioxolane) electropolymerized in polyacrylonitrile porous scaffolds: a novel composite polymer electrolyte for room temperature applications in safe solid-state lithium batteries, J. Power Sources Adv. 26 (2024) 100140, https://doi.org/10.1016/j.powera.2024.100140.
[36] Z. Wang, Y. Wang, L. Shen, Z. Jin, H.M. Law, A. Wang, W. Wang, F. Ciucci, Towards durable practical lithium–metal batteries: advancing the feasibility of poly-DOL-based quasi-solid-state electrolytes *via* a novel nitrate-based additive, Energy Environ. Sci. 16 (2023) 4084–4092, https://doi.org/10.1039/d3ee02020g.
[37] S. Zilinskaite, N. Reeves-McLaren, R. Boston, Xanthan gum as a water-based binder for P3-$Na_{2/3}Ni_{1/3}Mn_{2/3}O_2$, Front. Energy Res. 10, 909486. https://doi.org/10.3389/fenrg.2022.909486.
[38] A. Scalia, P. Zaccagnini, M. Armandi, G. Latini, D. Versaci, V. Lanzio, A. Varzi, S. Passerini, A. Lamberti, Tragacanth gum as green binder for sustainable water-processable electrochemical capacitor, ChemSusChem 14 (2021) 356–362, https://doi.org/10.1002/cssc.202001754.
[39] D. Versaci, O.D. Apostu, D. Dessantis, J. Amici, C. Francia, M. Minella, S. Bodoardo, Tragacanth, an exudate gum as suitable aqueous binder for high voltage cathode material, Batteries 9 (4) (2023) 199, https://doi.org/10.3390/batteries9040199.
[40] G. Lacarbonara, M. Sadd, J. Rizell, L. Bargnesi, A. Matic, C. Arbizzani, Operando insights into ammonium-mediated lithium metal stabilization: surface morphology modulation and enhanced SEI development, J. Colloid Interface Sci. 669 (2024) 699–711, https://doi.org/10.1016/j.jcis.2024.05.024.
[41] N.P.W. Pieczonka, Z. Liu, P. Lu, K.L. Olson, J. Moote, B.R. Powell, J.-H. Kim, Understanding transition-metal dissolution behavior in $LiNi_{0.5}Mn_{1.5}O_4$ high-voltage spinel for lithium ion batteries, J. Phys. Chem. C 117 (2013) 15947–15957, https://doi.org/10.1021/jp405158m.